

Epitaxial growth of the cubic L2₁-Mn_{2.6}Ga Heusler alloy on MgO(001)

Rocío M. Gutiérrez-Pérez¹, José T. Holguín-Momaca¹, Guo Tian², Shuchi Sunil Ojha²,
Ricardo López Antón³, Caroline A. Ross², and Sion F. Olive-Méndez^{1,a)}

¹*Centro de Investigación en Materiales Avanzados, S.C. (CIMAV) Miguel de Cervantes No. 120, C.P. 31136, Chihuahua, Chih., Mexico.*

²*Department of Materials Science and Engineering, Massachusetts Institute of Technology, 77 Massachusetts Avenue, Cambridge, MA 02139, USA*

³*Instituto Regional de Investigación Científica Aplicada (IRICA) and Departamento de Física Aplicada, Universidad de Castilla-La Mancha, 13071 Ciudad Real, Spain*

Electronic mail: sion.olive@cimav.edu.mx

Abstract

The Mn₃Ga Heusler alloy possesses different crystalline structures representing a range of properties of interest for spintronic applications. We report on the structural and magnetic characterization of the disordered cubic-fcc L2₁-Mn_{2.6}Ga thin films grown on MgO(001) substrates. The first two nanometers of thickness of the Mn_{2.6}Ga thin films are highly strained to the substrate with a lattice mismatch of 9.54%, playing the role of a template layer for the subsequent growth of relaxed L2₁-Mn_{2.6}Ga. Once the films reach a critical thickness of 15 nm, the cubic phase reorients its epitaxial relationship from a (001) to a (111) in-plane orientation. Magnetic measurements show that the samples exhibit perpendicular magnetic anisotropy and also that the usually antiferromagnetic L2₁-Mn₃Ga films are ferromagnetic with a Curie temperature > 400 K due to partially compensated Mn moments.

Keywords: Mn₃Ga, cubic L2₁, MgO(001), ferromagnetism.

Ferrimagnetic Heusler alloys are promising materials for spintronic applications and a wide range of compositions has been explored including $\text{Mn}_{1.5}\text{FeV}_{0.5}\text{Al}$, Cr_2MnSn , Mn_2CrGa , Co_2MnSi , and others.^{1,2,3,4} A low magnetization, strong perpendicular magnetic anisotropy and high Curie temperature are desirable for efficient switching via spin transfer torque (STT), enabling the realization of spintronic devices such as STT-magnetic random access memory.^{5,6,7}

Full Heusler alloys with formula X_2YZ , where X is the most electropositive element, can crystallize in the cubic L_{21} structure (space group $\text{Fm}\bar{3}m$)⁸. One example of these alloys is Mn_3Ga (where X and Y are Mn), which possesses different magnetic properties depending on its crystalline structure, stoichiometry, synthesis technique and growth temperature.^{9,10,11,12} In its most stable form, Mn_3Ga forms the tetragonal D_{022} crystalline structure with lattice constants $a = 3.94 \text{ \AA}$ and $c = 7.1 \text{ \AA}$ and ferrimagnetic ordering.¹³ A random distribution of the Mn and Ga atoms converts the unit cell of the D_{022} structure into two cubic unit cells of the disordered L_{21} antiferromagnetic phase. The L_{21} disordered fcc Mn_3Ga with lattice constant $a = 3.84 \text{ \AA}$ has been reported to be antiferromagnetic (AFM) with Néel temperature of 400 K.^{14,15} Early theoretical calculations show that the cubic structure is a transition phase during the transformation from tetragonal to hexagonal phases.¹⁶ Few works report the formation of this phase experimentally. Kharel et al.¹⁴ synthesized the $\text{L}_{21}\text{-Mn}_3\text{Ga}$ phase in the form of ribbons prepared by melt-spinning. The ribbons have thermal stability up to 350 °C, and above this temperature a transformation to the tetragonal- D_{022} and to the hexagonal- D_{019} phases is observed upon thermal annealing at 500 and 600 °C, respectively. Recently, Bang et al.¹⁵ reported the growth of $\text{L}_{21}\text{-Mn}_3\text{Ga}$ thin films by varying the power during magnetron sputtering. The cubic AFM phase is achieved only when the samples contain a Mn excess in the range 1-10 at.%.¹⁵ The AFM ordering arises from stacking alternating ferromagnetic (FM) planes along the c axis. The same authors reported that $\text{L}_{21}\text{-Mn}_3\text{Ga}$ thin films have poor metallic conductivity.¹⁷

In this article, we report on the growth using magnetron sputtering of cubic $\text{L}_{21}\text{-Mn}_{2.6}\text{Ga}$ films with 5 – 50 nm thicknesses on $\text{MgO}(001)$ substrates via a highly strained $\text{Mn}_{2.6}\text{Ga}$ ultrathin template layer. Structural analyses were performed in order to identify the evolution of the lattice parameter with the thickness of the film. The strained $\text{Mn}_{2.6}\text{Ga}$

template layer is a soft magnetic phase whereas the relaxed $\text{Mn}_{2.6}\text{Ga}$ phase exhibits partially uncompensated antiferromagnetism and has strong perpendicular anisotropy.

Epitaxial $\text{Mn}_{2.6}\text{Ga}$ thin films were grown in a magnetron sputtering system with a base pressure better than 5×10^{-8} Torr. The growth chamber is equipped with a reflection high-energy electron diffraction (RHEED) system operating at 30 kV. The film growth was carried out using a 2-inch diameter homemade Mn_3Ga target fabricated by magnetic induction heating. Square sections of a $\text{MgO}(001)$ wafer were degassed *in-situ* at 400 °C for 12 h; the substrate was held at this temperature during the thin film deposition. The Mn_3Ga target was sputtered using a radio-frequency power source at 35 W corresponding to a low deposition rate of 0.9 nm/min, which favors simultaneously the nucleation of the cubic phase and the achievement of a flat film surface. The chemical composition equal to $\text{Mn}_{2.6}\text{Ga}$ was evaluated by X-ray photoelectron spectroscopy (results not shown). **Higher sputter powers lead to an increase in the Mn content, with composition of Mn_3Ga at 75 W power.** The structural characterization of the layers was performed by RHEED, high-resolution transmission electron microscopy (HR-TEM) and X-ray diffractometry (XRD). The magnetic properties were characterized using magnetic force microscopy (MFM) and superconducting quantum interference device (SQUID) magnetometry.

Single crystal $\text{MgO}(001)$ substrates with a lattice constant of 4.212 Å (a mismatch of 9.54% with the a lattice constant of Mn_3Ga) were used for the growth of the thin films. The RHEED patterns of the surface of $\text{MgO}(001)$ taken along the [110] and [100] directions are shown in Figs. 1(a) and 1(b). The RHEED patterns of the surface of a 10 nm-thick relaxed $\text{Mn}_{2.6}\text{Ga}$ film along the [110] and [100] directions are shown in Figs. 1(c) and 1(d). The well-defined and ordered spots observed on the diffraction patterns indicate epitaxial growth. The general shape of the diffraction spots of the surface of the $\text{Mn}_{2.6}\text{Ga}$ thin films remains unchanged up to a thickness of 15 nm; the only evolution is the separation of the diffraction spots of the $\text{Mn}_{2.6}\text{Ga}$ layers on the (001) plane, i.e. along the [110] and [100] directions. This is depicted in Figs. 1(a) and 1(c) by the blue and yellow lines, which represent the interatomic distances in reciprocal space of the substrate and those of a 10 nm thick film. The separation of the 1×1 order spots of the RHEED pattern along the [100] direction in Fig. 1(d) was used to measure the evolution of the lattice constant of the film at the growth front within a standard deviation of 0.018 Å. Figure 1(e) shows the evolution of

the lattice constant a of the film along the [100] direction for the first 5 nm thickness showing a gradual change from the lattice constant of MgO = 4.212 Å to a relaxed value of 3.84 Å at a thickness of 2 nm. Beyond this thickness, the lattice constant remained unchanged corresponding to the cubic Mn₃Ga with a bulk lattice constant of 3.84 Å. Based on the RHEED diffraction patterns, we identify the epitaxial relationship for the L2₁ phase of Mn₃Ga and for film thicknesses less than 15 nm: MgO(001)[100]||Mn_{2.6}Ga(001)[100].

The phase identification of the samples with different thicknesses was also examined by XRD in a Bragg-Brentano configuration as shown in the set of diffraction patterns in Fig. 1(f). The XRD pattern of a bare substrate is also included for comparative purposes. The diffraction pattern of the sample with a thickness of 10 nm consists of only a broad peak centered at ~47.5° which is near the predicted position of the (002) peak of the cubic phase (47.3°). However, due to the lattice distortion (in-plane expansion and out-of-plane compression) of the Mn_{2.6}Ga layer at the early growth stages, this phase may be described as tetragonally distorted.

The XRD pattern of a film with a thickness of 15 nm shows the coexistence of the D0₂₂ and the L2₁ phases, where the cubic (002) peak is the one with the highest intensity. It is possible that some mosaicity leads to an increase of the signal of the tetragonal D0₂₂ phase, whose visible peaks are indexed to (004) ($2\theta \sim 50^\circ$, compared to bulk $2\theta = 51.5^\circ$) and (002). Additionally, a peak appears at $2\theta = 38.8^\circ$, which became more intense as the thickness increases. This peak corresponds to the L2₁-(111) peak and suggests that the cubic phase undergoes a change in epitaxial relationship beyond a critical thickness of ~15 nm. The change in structure will be later correlated with the TEM observations. For a 50-nm thick film, the intensity of this (111) peak equals the intensity of the (002) peak, and is shifted to a higher angle of 39.9°. The formation of the hexagonal D0₁₉ phase is discounted because its (0002) peak would be at $2\theta \sim 41.4^\circ$ ($a = 5.404$ Å, $c = 4.357$ Å [6]).

Figure 2(a) shows a low magnification TEM micrograph of the Mn_{2.6}Ga layer. Based on the results of the XRD and RHEED analysis, we can compare the thickness at which the (111) orientation of L2₁-Mn_{2.6}Ga (and the minority tetragonal D0₂₂ phase) appears. This transition is observed as a thin dark contrast on the micrograph; although this interface is smooth, further growth of the Mn_{2.6}Ga leads to a higher surface roughness. The low

deposition rate appears to be important in promoting the epitaxial reorientation, and increasing the deposition rate suppresses the (111) peak in 50 nm thick films.

Fig. 2(b) shows the raw HR-TEM micrograph and Fig. 2(c) shows the right side of the micrograph subjected to a fast Fourier transform (FFT) filtering process. The following analysis, i.e., the measurements of the lattice constants, was performed on the raw image in order to avoid any errors due to the FFT. In both figures, the bottom dotted line indicates the MgO/Mn_{2.6}Ga interface where the in-plane period measured from a line profile scan is 4.2 Å in agreement with the in-plane lattice constant of the substrate. The crystalline directions of the substrate and film were identified from the FFT pattern (not shown) and corroborate the epitaxial relationship deduced previously. A second interface has been drawn at the position where the *a* lattice constant of the film reaches 3.81 Å, close to the bulk value of 3.84 Å for the disordered L2₁-Mn₃Ga. The interfaces are semicoherent with misfit dislocations indicated by the symbol ⊥. The growth mode differs from that of Bang et al.¹³, which exhibited domain-matching epitaxy with a ratio of 10:9 Mn₃Ga:MgO unit cells at the interface, and a rough film surface corresponding to the domain boundaries. Bang et al.¹⁵ also found that the cubic phase was favored at lower growth rates but transitioned to mixed then tetragonal films at higher growth rates and lower Mn content.

The combination of low deposition rate and the relatively high substrate temperature (400 °C) enabled the formation of a well-crystallized thin film with a RMS surface roughness of 1.9 nm as shown in the 2 × 2 μm² atomic force micrograph in Fig. 3(a). Over the same surface area, a magnetic tip was used to scan the shape and distribution of the magnetic domains. Figure 3(b) shows the bright (dark) contrast that indicates up (down) oriented domains perpendicular to the film plane. The maze-like distribution of the magnetic domains is consistent with the PMA of the film. The width of the magnetic domains is about 100 nm and their length is 100 - 500 nm.

The in-plane (IP) and out-of-plane (OP) SQUID *M-H* loops of samples with various thicknesses are shown in Figs. 3(c) - 3(e). All magnetic loops, measured at 300 K, show a dominant PMA with a saturation magnetization (*M_s*) of 90 kAm⁻¹ for the 5 nm thick film and *M_s* = 100 kAm⁻¹ for thicker films. The 5 nm thick film exhibits *M-H* loops without hysteresis in both IP and OP orientations indicating that at this thickness the material behaves as a soft magnet.^{18,19} For the 20 nm and 50 nm thick films there is a step in the OP

M - H loops (indicated by an arrow in Fig. 3(d) and 3(e)), indicating the presence of two magnetic phases, one soft and the other hard, with different switching fields. Further analysis of the M - H curves is shown in Fig. 3(f) where the magnetic moment of the 5 nm thick film has been subtracted from the raw magnetic moments of the thicker films. The resulting M - H curves have no low-field step, which suggests that the step corresponds to the magnetic moment of the first part of the film, which includes the strained layer. Therefore, the magnetometry data suggest that the strained $L2_1$ layer is magnetically soft, whereas for films with thicknesses ≥ 20 nm, the overlying $L2_1$ phase (both (001) and (111) oriented) plus the minority of tetragonal phase is magnetically hard. The (111)-oriented region has its easy axis tilted with respect to the film plane, which may account for the loop opening in the IP data.

The films exhibit strong PMA with K_u of 0.70 and 0.65 MJm⁻³ for thicknesses of 20 and 50 nm, respectively. The anisotropy constant K_u was calculated from the expression $K_u = \mu_0 M_s H_a / 2$, where H_a is the saturation field in the hard axis.

The behavior of the soft layer in the 50 nm film is examined in more detail by measuring minor loops after saturating the sample at 5 T then applying demagnetizing fields of -0.2, -0.06 and 0.0 T as shown in Fig. 3(g-h). The minor loops show hysteresis not seen in the loop of the 5 nm thick film, suggesting that a magnetic interaction between the hard and soft layers may stabilize reverse domains formed in the soft layer.

The soft behavior of the strained layer and hard behavior of the overlying layer differ from prior reports of antiferromagnetism in the cubic phase [Ref. 15]. The difference may be due to the effects of composition and strain. AFM coupling in metallic Mn-based alloys occurs for interatomic distances < 2.9 Å. Considering that the interatomic distances of the first nearest neighbors in the disordered $L2_1$ phase is $\sqrt{2}a/2 = 2.71$ Å, AFM behavior is expected. However, the Mn deficiency in our samples (with a composition of $Mn_{2.6}Ga$, i.e. the average unit cell contains 2.89 Mn and 1.11 Ga atoms) leads to Ga_{Mn} antisite defects, weakening the AFM interactions and leading to a net moment due to uncompensated antiferromagnetism. The magnetic moment per Mn atom in the $L2_1$ phase estimated by theoretical calculations is 2.46 μ_B/Mn [Ref. 14]. However, in our samples, $M_s = 100$ kAm⁻¹ corresponds to a magnetic moment of 1.83 $\mu_B/f.u.$, i.e. less than one moment of a Mn atom per fcc unit cell is uncompensated. Finally, a M - T curve was performed (not shown) to

evaluate the Curie temperature (T_c) of the films. The curve shows a monotonically decreasing magnetization with increasing temperature, and the T_c is higher than 400 K. Ref. 15 reported $T_c = 800$ K for tetragonal Mn_3Ga .

In summary, we have grown epitaxial $\text{Mn}_{2.6}\text{Ga}$ thin films on $\text{MgO}(001)$ substrates with different thicknesses. At the initial growth stages a highly strained layer nucleates and takes the role of a template layer for the further growth of the cubic disordered L_{21} phase. The strained layer with a thickness of 2 nm behaves as a soft magnet, whereas the layer with the L_{21} crystal structure grown on the strained template layer behaves as a hard magnet with a high perpendicular magnetic anisotropy with uniaxial anisotropy constants of 0.7 and 0.65 MJm^{-3} for films with total thicknesses of 20 and 50 nm. Our findings show that a Mn deficiency with respect to the ideal stoichiometry of $\text{L}_{21}\text{-Mn}_3\text{Ga}$ leads to a net magnetic moment, assumed to arise from uncompensated antiferromagnetism. Magnetic force microscopy images revealed maze-like out-of-plane oriented magnetic domains. The low magnetization and the high perpendicular anisotropy of $\text{L}_{21}\text{-Mn}_{2.6}\text{Ga}$ films suggest their use in spintronic applications (such as magnetic tunnel junctions based on exchange biased stacks of $\text{Mn}_3\text{Ga}/\text{Mn}_{2.6}\text{Ga}$) and motivate further control of properties by engineering their strain and composition.

The authors gratefully acknowledge financial support from the MIT-Mexico-CONACYT seed fund and the Spanish JCCM (project PEII-2014-042-P, FEDER, EU) and from the Plan Propio de la Universidad de Castilla-La Mancha (FEDER, EU) for the “Grupo de Materiales Magnéticos (GMM)”. CAR acknowledges the SMART Center, a Semiconductor Research Corporation nCORE center sponsored by the National Institute of Standards and Technology.

Figure Captions

Fig. 1. RHEED patterns of the surface of the $\text{MgO}(001)$ substrate along the (a) $[110]$ and (b) $[100]$ directions. The RHEED patterns in (c) and (d) correspond to the relaxed surface of a 10 nm-thick $\text{Mn}_{2.6}\text{Ga}$ thin film. The blue and yellow lines in panels in (a) and (c) indicate the lattice mismatch between the substrate and film. (e) The evolution of the a

lattice constant of $\text{Mn}_{2.6}\text{Ga}$ shows a relaxation at 2 nm thickness. (f) XRD patterns of $\text{Mn}_{2.6}\text{Ga}$ thin films at different thicknesses.

Fig. 2. (a) Low magnification TEM micrograph of a 50 nm thick $\text{MgO}(001)/\text{Mn}_{2.6}\text{Ga}$ thin film showing the different layers of $\text{Mn}_{2.6}\text{Ga}$ (the (001) cubic and the (111) cubic plus minority tetragonal) separated by a darker grey line of contrast. HR-TEM micrographs: (b) raw micrograph and (c) filtered micrograph using the FFT process. The dotted lines indicate the interfaces with the substrate and between the strained and relaxed $\text{Mn}_{2.6}\text{Ga}$. The (\perp) symbols indicate misfit dislocations.

Fig. 3. (a) Atomic force and (b) magnetic force micrographs of the surface of a 50 nm-thick $\text{Mn}_{2.6}\text{Ga}$ thin film. SQUID M - H loops of thin films with thicknesses of (c) 5 nm, (d) 20 nm and (e) 50 nm. The arrows in (d) and (e) indicate the step between the switching fields of the strained and relaxed regions of $\text{Mn}_{2.6}\text{Ga}$. (f) Magnetic OP loops of the samples in panels (d) and (e) after subtracting the magnetic moment of the 5-nm thick film. (g) Minor curves at different demagnetizing fields and (h) a magnification of the minor curves showing hysteresis.

References

- ¹ R. Stinshoff, A. K. Nayak, G. H. Fecher, B. Balke, S. Ouardi, Y. Skourski, T. Nakamura, and C. Felser, Completely compensated ferrimagnetism and sublattice spin crossing in the half-metallic Heusler compound $\text{Mn}_{1.5}\text{FeV}_{0.5}\text{Al}$. *Phys. Rev.* 95, 060410(R) (2017).
- ² S. Gupta, F. Matsukura, and H. Ohno, Properties of sputtered full Heusler alloy Cr_2MnSb and its application in a magnetic tunnel junction. *J. Phys. D: Appl. Phys.* 52 (2019) 495002.
- ³ W. Zhang, Y. Jin, R. Skomski, P. Kharel, X. Li, T. Chen, G. Zhao, D. Kim, S. Valloppilly and D. J. Sellmyer, Mn_2CrGa -based Heusler alloys with low net moment and high spin polarization. *J. Phys. D: Appl. Phys.* 51 (2018) 255001.
- ⁴ N. Rabie, G. R. Gordani, and A. Ghasem, Enhancement of magnetic properties of Co_2MnSi Heusler alloy prepared by mechanical alloying method. *Journal of Magnetism and Magnetic Materials* 434 (2017) 135-142.
- ⁵ J. Winterlik, S. Chadov, A. Gupta, V. Alijani, T. Gasi, K. Filsinger, B. Balke, G. H. Fecher, C. A. Jenkins, F. Casper, J. Kübler, Guo-Dong Liu, Li Gao, S. S. P. Parkin, and Claudia Felser, Design scheme of new tetragonal heusler compounds for spin-transfer torque applications and its experimental realization, *Adv. Mater.* 24, 6283 (2012).

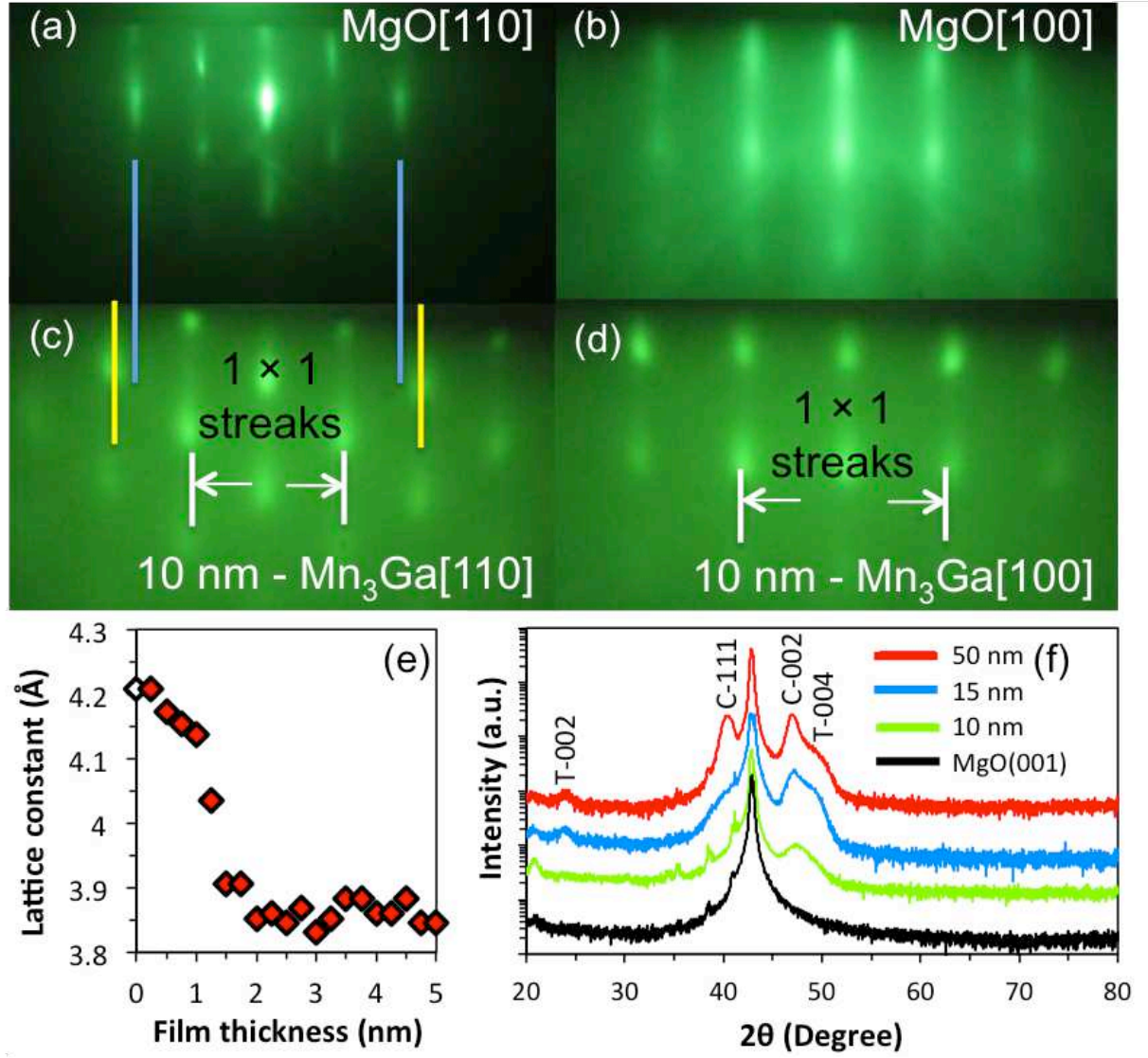
This is the author's peer reviewed, accepted manuscript. However, the online version of record will be different from this version once it has been copyedited and typeset.

PLEASE CITE THIS ARTICLE AS DOI: 10.1063/5.0001349

- ⁶ K. Z. Suzuki, R. Ranjbar, J. Okabayashi, Y. Miura, A. Sugihara, H. Tsuchiura, and S. Mizukami, Perpendicular magnetic tunnel junction with a strained Mn-based nanolayer, *Sci. Rep.* **6**, 30249 (2016).
- ⁷ X. P. Zhao, J. Lu, S. W. Mao, Z. F. Yu, D. H. Wei, and J. H. Zhao, Spin-orbit torque induced magnetization switching in ferrimagnetic Heusler alloy $D0_{22}$ - Mn_3Ga with large perpendicular magnetic anisotropy, *Appl. Phys. Lett.* **115**, 142405 (2019).
- ⁸ H. Kurt, K. Rode, M. Venkatesan, P. Stamenov, and J. M. D. Coey, High spin polarization in epitaxial films of ferrimagnetic Mn_3Ga , *Physical Review B*, **83**, 020405 (2011).
- ⁹ L. Zhu, S. Nie, K. Meng, D. Pan, J. Zhao, and H. Zheng, Multifunctional $L1_0$ - $Mn_{1.5}Ga$ films with ultrahigh coercivity, giant perpendicular magnetocrystalline anisotropy and large magnetic energy product, *Adv. Mater.* **24**, 4547 (2012).
- ¹⁰ F. Wu, S. Mizukami, D. Watanabe, H. Naganuma, M. Oogane, Y. Ando, and T. Miyazaki, Epitaxial $Mn_{2.5}Ga$ thin films with giant perpendicular magnetic anisotropy for spintronic devices, *Appl. Phys. Lett.* **94**, 122503. (2009).
- ¹¹ W. Feng, Y. Shin, S. Cho, and D. D. Dung, Growth-temperature-dependent ferrimagnetism in Mn_3Ga thin films, *J. Korean Phys. Soc.* **63**, 1055 (2013).
- ¹² J. Karel, F. Casoli, L. Nasi, P. Lupo, R. Sahoo, B. Ernst, A. Markou, A. Kalache, R. Cabassi, F. Albertini, and C. Felser, Enhanced magnetization and anisotropy in Mn-Ga thin films grown on LSAT, *Appl. Phys. Lett.* **111**, 182405 (2017).
- ¹³ H. Kurt, K. Rode, M. Venkatesan, P. Stamenov, and J. M. D. Coey, $Mn_{3-x}Ga$ ($0 \leq x \leq 1$): Multifunctional thin film materials for spintronics and magnetic recording, *Phys. Status Solidi (b)* **248**, 2338 (2011)
- ¹⁴ P. Kharel, Y. Huh, N. Al-Aqtash, V. R. Shah, R. F. Sabirianov, R. Skomski and D. J. Sellmyer, Structural and magnetic transitions in cubic Mn_3Ga , *J. Phys.: Condens. Matter* **26**, 126001 (2014).
- ¹⁵ H.-W. Bang, W. Yoo, C. Kim, S. Lee, J. Gu, Y. Park, K. Lee, and M.-H. Jung, Structural, Magnetic, and electrical properties of collinear antiferromagnetic heteroepitaxy cubic Mn_3Ga thin films, *Appl. Phys. Lett.* **115**, 012402 (2019).
- ¹⁶ D. Zhang, B. Yan, S.-C. Wu, J. Kübler, G. Kreiner, S. S. P. Parkin and C. Felser, First-principles study of the structural stability of cubic, tetragonal and hexagonal phases in Mn_3Z ($Z = Ga, Sn$ and Ge) Heusler compounds, *J. Phys.: Condens. Matter* **25**, 206006 (2013).
- ¹⁷ Y. Jang, W. Yoo, H.-W. Bang, C. Kim, Y. Haeng Lee, K. Lee, M.-H. Jung, Gradual phase transition from ferromagnetic tetragonal to antiferromagnetic cubic states in Mn_xGa ($1.80 \leq x \leq 3.03$) thin films, *J. Alloys Compd.* **810**, 151988 (2019).
- ¹⁸ B. S. Yang, L. N. Jiang, W. Z. Chen, P. Tang, J. Zhang, X.-G. Zhang, Y. Yan, and X. F. Han, First-principles study of perpendicular magnetic anisotropy in ferrimagnetic $D0_{22}$ - Mn_3X ($X = Ga, Ge$) on MgO and $SrTiO_3$, *Appl. Phys. Lett.* **112**, 142403 (2018).
- ¹⁹ Albrecht Köhler, Ivan Knez, Daniel Ebke, Claudia Felser, and Stuart S. P. Parkin, Loss of anisotropy in strained ultrathin epitaxial $L1_0$ Mn-Ga films, *Appl. Phys. Lett.* **103**, 162406 (2013).

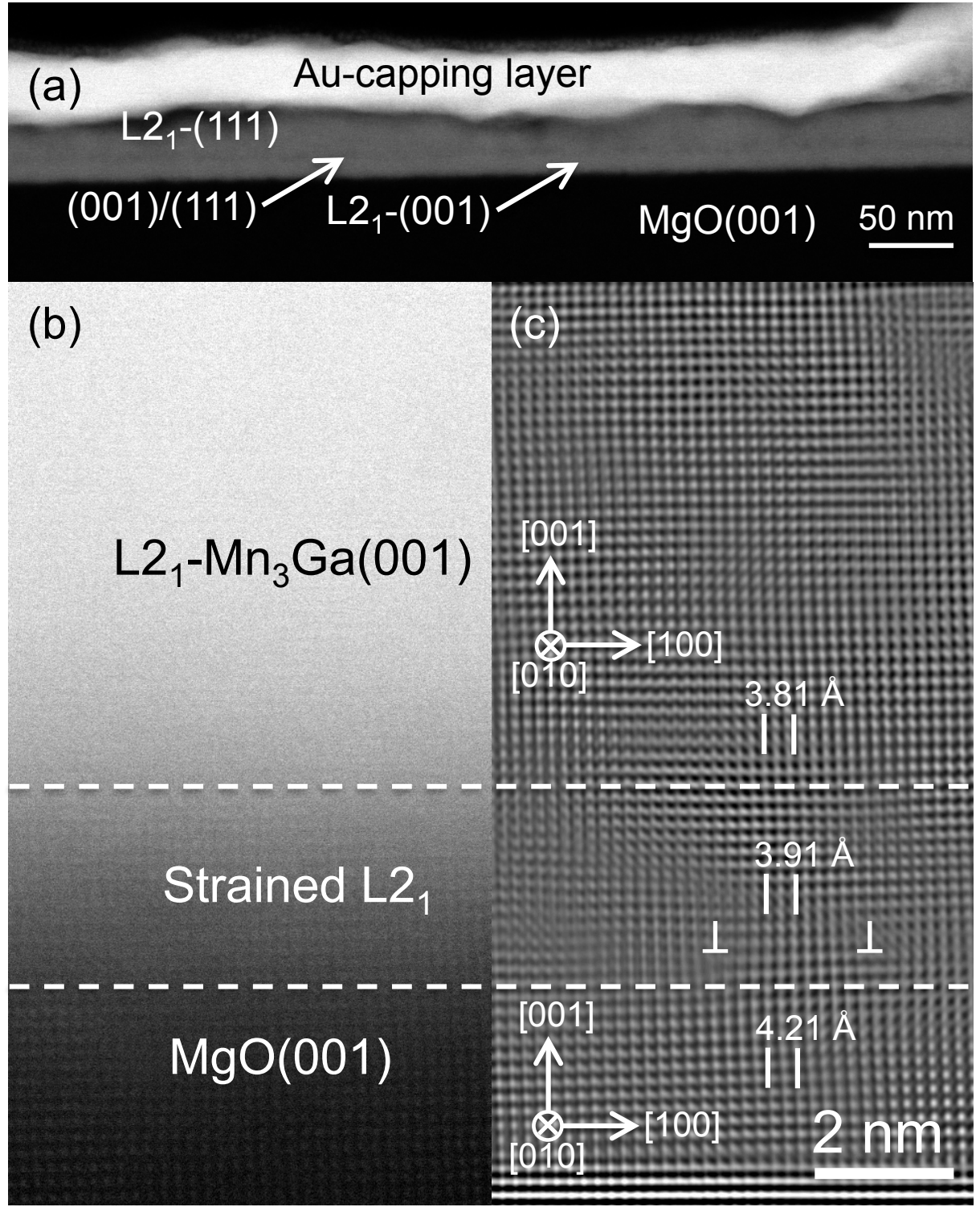
This is the author's peer reviewed, accepted manuscript. However, the online version of record will be different from this version once it has been copyedited and typeset.

PLEASE CITE THIS ARTICLE AS DOI: 10.1063/5.0001349



This is the author's peer reviewed, accepted manuscript. However, the online version of record will be different from this version once it has been copyedited and typeset.

PLEASE CITE THIS ARTICLE AS DOI: 10.1063/5.0001349



This is the author's peer reviewed, accepted manuscript. However, the online version of record will be different from this version once it has been copyedited and typeset.

PLEASE CITE THIS ARTICLE AS DOI: 10.1063/5.0001349

